Retrieval of the optical properties of a semiinfinite compartment in a layered scattering medium by single-distance, time-resolved diffuse reflectance measurements

H.A. García [a,*], D.I. Iriarte [a], J.A. Pomarico [a], D. Grosenick [b], R. Macdonald [b]

[a] IFAS (UNCPBA) and CIFICEN (UNCPBA – CICPBA – CONICET), Pinto 399, B7000GHG Tandil, Bs. As., Argentina
[b] Physikalisch – Technische Bundesanstalt (PTB), Abbestr. 2-12, 10587 Berlin, Germany

ARTICLE INFO

ABSTRACT

Functional analysis of the human brain requires methods that take the layered structure of the head into account. In this work we introduce an improved theoretical model that describes light propagation in multilayered, turbid cylinders with a infinitely thick bottom layer, which simplifies calculations and reduces computation times. Our approach was validated with Monte Carlo simulations and single distance, time-resolved experiments on a three-layered phantom, where the absorption of the deepest layer was gradually modified. We were able to retrieve both, the scattering and absorption coefficient of this layer within reasonable errors. Hereby, changes in scattering were found to have less effect on the experimental data than absorption changes, making the reliable estimation of the reduced scattering coefficient more difficult in comparison to absorption. Stability of the implemented fitting routine was thoroughly analyzed, revealing that special care is needed to obtain accurate values for the reduced scattering coefficient.

1. Introduction

Since the first applications of NIR light to non-invasive studies of brain activity [1], great efforts have been made to understand how optical radiation propagates in tissue and interacts with the different constituents of the head. The first and simplest models consider this region of the body as an optically homogeneous medium where light propagates under the diffusive regime. This is, of course, a rather unreal approximation, since the head is formed, among other things, by the scalp, skull, cerebrospinal fluid (CSF), white matter and gray matter [2–4], all of which can be considered as layers of a definite depth. In the past 20 years different models were presented describing light propagation through layered systems [5–10]. Among these, the one developed by Kienle and Liemert [11] describes NIR photon migration through N-layered cylinders of finite axial extension, making calculations much more simpler and faster than those involved when considering semiinfinite media or finite parallelepipeds in planar cartesian coordinates [10]. In the case of two-layered systems, Hallacoglu et al. [12] showed that it is possible to use this model, together with several source-detector distances, in a fitting

algorithm to retrieve the optical properties (absorption coefficient, μ_a, and reduced scattering coefficient, μ'_s) of both layers, as well as the thickness of the first one. They apply their method to Monte Carlo simulations, phantoms and human foreheads, with deviations in the first two cases of less than 10%.

Recently, Martelli et al. [13] discussed the estimation of the optical properties of a two-layer phantom from time-resolved measurements using a single source-detector distance. They were able to retrieve the full set of optical properties together with the thickness of the upper layer when a Bayesian approach was applied. The success of this approach is mainly based on the assumption of expectation values already very close to the true parameters. Having the large variability of biological tissue in mind, the pre-selection of such expectation values seems problematic. Moreover, when considering investigations on the brain, the two-layer model is a comparably strong simplification of the true tissue geometry.

In the present work we investigate the influence of the optical properties of a hidden layer on time-resolved measurements at selected source-detector distances. We discuss the significance of the absorption and reduced scattering coefficient on the shape of the distribution of times of flight, which gives us insight in the possibilities and limitations to derive the optical properties from single distance measurements by fitting. Having obtained this knowledge, we compare the retrieval of the hidden layer optical

* Corresponding author.
E-mail address: hgarcia@exa.unicen.edu.ar (H.A. García).

properties with a standard Levenberg-Marquardt approach for several source-detector distances. The theoretical model for our analysis is based on the contribution from Ref. [11]. It considers a turbid cylinder consisting of a number of finite layers on top of a infinitely thick one. In our experimental verification we use a three-layered phantom as a model for the layered structure of the brain. By assuming prior knowledge in the optical properties of the upper two layers we focus on the effects of the layer of interest, thus avoiding additional uncertainties arising from the upper layers [14–16].

This publication is structured as follows. In Section 2 we discuss our theoretical model. In Section 3 we introduce the experimental setup and the fitting algorithm for retrieving the optical parameters of the deepest layer, and we also describe the Monte Carlo simulations used to validate our model numerically. In Section 4 we present the results obtained for different source-detector separations and we also discuss the reliability of the retrieved absorption and scattering properties. Finally, in Section 5 we present the main conclusions and future work.

2. Theoretical considerations

We consider an N – layered turbid cylinder of radius R, as shown in Fig. 1. Layer j has optical properties $\mu_{a,j}$ and $\mu'_{s,j}$, refractive index n_j and thickness l_j except for the last layer, which is taken as having an infinite thickness. The origin of the coordinates system is located at the center of the top surface. A beam-like source impinges on the cylinder at point $(\rho, \varphi, z) = (0, 0, 0)$; according to the diffusion approximation [17] it is considered as an isotropic point source at a depth $z_0 = (\mu'_{s,1})^{-1}$, i.e. the actual point source position is $\mathbf{r_0} = (0, 0, z_0)$.

Following Ref. [11], we first treat the problem in the frequency domain, and after that we sum over a high number of frequencies to obtain the corresponding time domain expression by inverse Fourier transformation. The Diffu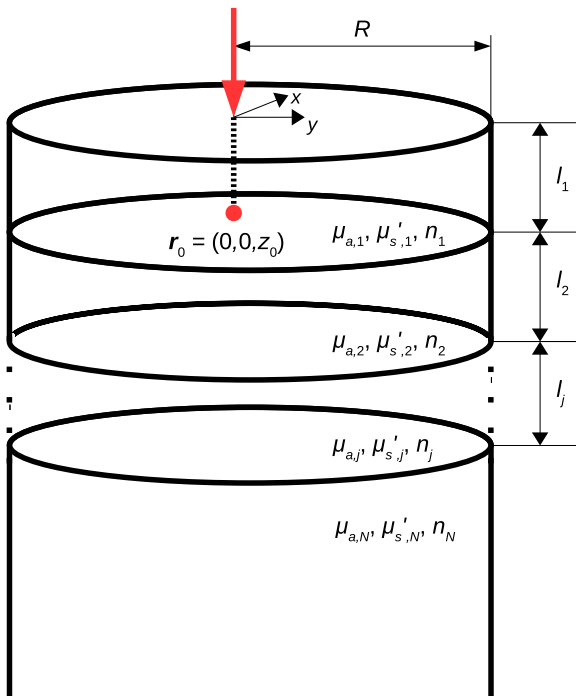sion Equation (DE) for the fluence rate $\Phi(\rho, z, \omega)$ in the first layer, in cylindrical coordinates, is given by:

$$\left[\left(\frac{\partial^2}{\partial\rho^2} + \frac{1}{\rho}\frac{\partial}{\partial\rho} + \frac{\partial^2}{\partial z^2}\right) - \left(\frac{\mu_{a,1}}{D_1} + i\frac{\omega}{D_1 c_1}\right)\right]\Phi(\rho, z, \omega)$$
$$= -\frac{1}{D_1\rho}\delta(\rho - \rho_0)\delta(z - z_0), \tag{1}$$

where $D_1 = (3\mu'_{s,1})^{-1}$ and c_1 are the diffusion coefficient and the speed of light in the first layer, respectively, and ω is the frequency of the modulated light. We have omitted the angular dependence in Eq. (1) because of the cylindrical symmetry. This equation is valid for the layer including the source; the diffusion in all the other layers is described by a homogeneous version of Eq. (1).

Applying the Extrapolated Boundary Condition (EBC) it is possible to find that the fluence vanishes at a distance $z_{b,1} = 2AD_1$ above the top surface, with A being a factor that depends on the refractive indexes of both the turbid and the surrounding media [18] . This boundary condition is used together with the following transform:

$$\Phi(s_n, \omega, z) = \int_0^{R_{EBC}} \rho\Phi(\rho, z, \omega)J_m(s_n\rho)d\rho, \tag{2}$$

where J_m is the Bessel function of the first kind and order m, $R_{EBC} = R + z_{b,1}$ and s_n satisfies the relation:

$$J_m(R_{EBC}s_n) = 0, \tag{3}$$

with $n = 1, 2, 3....$ Applying transform (2) to equation (1), the following ordinary differential equation is obtained:

$$\left[\frac{d^2}{dz^2} - \alpha_1^2\right]\Phi = -\frac{1}{D_1}J_m(s_n\rho_0)\delta(z - z_0), \tag{4}$$

being $\alpha_1^2 = \frac{\mu_{a,1}}{D_1} + s_n^2 + i\frac{\omega}{D_1 c_1}$. The Green's function that satisfies the whole system is:

$$G_1(s_n, \omega, z) = A_1 e^{\alpha_1 z} + B_1 e^{-\alpha_1 z} + \frac{e^{-\alpha_1|z-z_0|}}{2D_1\alpha_1},$$
$$G_k(s_n, \omega, z) = A_k e^{\alpha_k z} + B_k e^{-\alpha_k z}, \tag{5}$$

for the 1st and the kth layer, with $k > 1$, respectively. The boundary conditions that determine the remaining constants are:

$$G_1(s_n, \omega, z = -z_{b,1}) = 0,$$
$$n_{k+1}^2 G_k(s_n, \omega, z = L_k) = n_k^2 G_{k+1}(s_n, z = L_k, \omega),$$
$$D_k \frac{\partial G_k(s_n, z, \omega)}{\partial z}\bigg|_{z=L_k} = D_{k+1}\frac{\partial G_{k+1}(s_n, z, \omega)}{\partial z}\bigg|_{z=L_k},$$
$$G_N(s_n, z \to \infty, \omega) = 0, \tag{6}$$

where $L_k = \sum_{i=1}^k l_i$, with $k = 1, 2, ..., N$. Then, the Green's function for the 1st layer is:

$$G_1(s_n, \omega, z) = \frac{e^{-\alpha_1|z-z_0|} - e^{-\alpha_1(z+z_0+2z_{b,1})}}{2D_1\alpha_1}$$
$$+ \frac{\sinh[\alpha_1(z_0 + z_{b,1})]\sinh[\alpha_1(z + z_{b,1})]}{D_1\alpha_1 e^{\alpha_1(l_1+z_{b,1})}}$$
$$\times \frac{D_1\alpha_1 n_1^2\beta_N - D_2\alpha_2 n_2^2\gamma_N}{D_1\alpha_1 n_1^2\beta_N \cosh[\alpha_1(l_1 + z_{b,1})] + D_2\alpha_2 n_2^2\gamma_N \sinh[\alpha_1(l_1 + z_{b,1})]}. \tag{7}$$

The essential difference with respect to Ref. [11], due to the last boundary condition in (6), is the form of β_N and γ_N:

$$\beta_N = D_{N-1}\alpha_{N-1}n_{N-1}^2\cosh(\alpha_{N-1}l_{N-1}) + D_N\alpha_N n_N^2\sinh(\alpha_{N-1}l_{N-1}), \tag{8}$$

Fig. 1. N-layered turbid cylinder with an infinitely thick last compartment.

$$\gamma_N = D_{N-1}\alpha_{N-1}n_{N-1}^2 \sinh(\alpha_{N-1}l_{N-1}) + D_N\alpha_N n_N^2 \cosh(\alpha_{N-1}l_{N-1}). \quad (9)$$

These expressions are easier to handle since they do not include any terms depending on the thickness of the last layer. However, taking into account very thick layers is a problem in the model of Ref. [11], since the quantity $\alpha_N l_N$ appears as the argument of hyperbolic functions, which, assuming typical optical properties, easily diverge even for values of l_N larger than 20 mm.

The time domain fluence rate $\Phi_1(\mathbf{r}, t)$ can be obtained applying the inverse Fourier transform and the inverse finite Hankel transform [19] to equation (7):

$$\Phi_1(\mathbf{r}, t) = \frac{1}{2\pi^2 R_{EBC}^2} \sum_{n=1}^{\infty} \left[\int_{-\infty}^{\infty} G_1(s_n, z, \omega)e^{i\omega t}d\omega \right] \frac{J_0(s_n\rho)}{J_1^2(s_n R_{EBC})}. \quad (10)$$

Finally, the reflectance $R(\rho, t)$ at the surface $z=0$ and at a distance $\rho = \sqrt{x^2 + y^2}$ from the cylinder axis is calculated as follows[1][20]:

$$R(\rho, t) = \frac{\Phi_1(\rho, z = 0, t)}{2A}. \quad (11)$$

3. Experiments and simulations

3.1. Experiments on phantoms

In order to validate the model introduced in Section 2, single distance, time-resolved reflectance experiments were performed on a three-layered phantom, as shown in Fig. 2. We consider this is a better situation compared to the case of two layers, since it is more adequate for understanding how light travels to deeper tissue in a real human head, due to the detailed absorption and scattering characteristics of each of the upper tissues. All the layers were prepared with a mix of milk (as a dispersion agent) and water (as carrier) in the following proportion: $1l_{water}$: $0.26l_{milk}$. The phantom consisted of two thin solid layers and a liquid layer resembling a semiinfinite tissue compartment, which optical properties are of interest (see also Tables 1 and 2 in Section 4). To obtain the solid layers, 2% of agarose was added to the milk-water solution. Besides, India ink was added to all layers, to achieve the desired absorption properties for each of them. In the case of the solid layers, the ink concentration remained fixed, while in the liquid layer it was varied in order to control the optical absorption coefficient. For the preparation of the solid layers we followed the instructions presented in Ref. [22], which mainly consisted in heating the solution of water and agarose up to 95 °C, then pouring the desired volume of milk and ink, and finally stirring the mixture to guarantee homogeneity, until reaching 45 °C, when it properly begin to solidify.

The phantom was mounted upside down, inside a black, plastic cuvette of dimensions 150 mm x 120 mm x 70 mm and with the semiinfinite layer (the liquid one) at the top (Figs. 2 and 3). The illumination and detection optical fibers were inserted at the bottom (Fig. 2) through proper holes. With this setup, the liquid layer was easily accessible from the top, allowing both: i) to

---

[1] Although this expression is deduced for a slab geometry, numerical results show to be very similar to the ones given by the more formal equation relating fluence and flux [21]:

$$R(\rho, t) = \frac{1}{4\pi} \int_{2\pi} d\Omega \left[1 - R_f(\theta) \right]$$
$$\times \left[\phi_1(\rho, z = 0, t) + 3D_1 \frac{\partial \Phi_1(\rho, z, t)}{\partial z}\bigg|_{z=0} \cos\theta \right] \cos\theta,$$

where $R_f(\theta)$ is the Fresnel reflection coefficient for an incident angle θ. As well as this, it is much easier to program and faster to run.
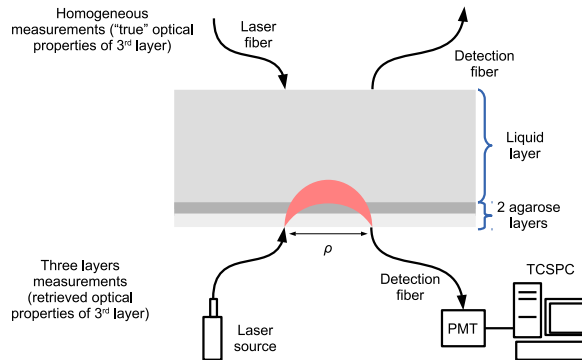

Fig. 2. Scheme of the experimental setup for measuring the optical properties of the deepest layer in the three-layered phantom.
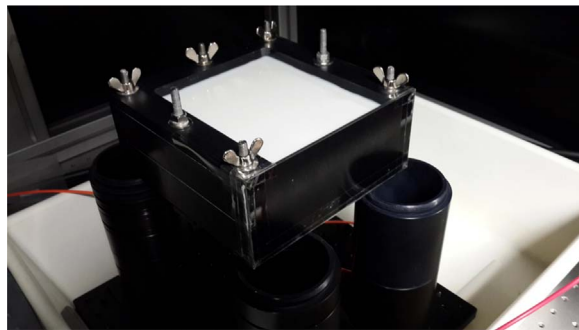

Fig. 3. Black cuvette containing the two solid layers at the bottom and the liquid one on top. The input and output light fibers were connected to the bottom face.

introduce the desired changes in the absorption coefficient with minimum interaction with the phantom; and ii) direct measurements of its optical properties for each ink concentration, without interaction with the agarose layers. The optical properties of the two solid (shallower) layers were measured in a separate experiment using the same mixture but in slabs thick enough to fulfill the requirements needed for satisfying the homogeneous model used to fit the resulting DTOFs [18]. In this way, the "true" optical properties of every layer forming the whole phantom could be known separatedly before the three layers experiment was performed.

As stated before, the aim of this experiment was to retrieve the optical properties of the liquid layer in the three-layered configuration. To this end we used a pulsed laser source (Spectra-Physics Mai Tai, pulse width <100 fs, $\lambda = 780$ nm, repetition rate 80 MHz, power drift $< \pm 1\%$ in any two-hour period, $P=110$ mW at the phantom) impinged onto the first solid layer at the bottom of the system, and the diffusively reflected photons gathered at the detection fiber were detected by a time correlated single photon counting (TCSPC) system to build up the corresponding distributions of times of flight (DTOFs). We changed the absorption coefficient of the liquid layer by using six ink concentrations, and measured the whole system with three different source-detector distances, namely $\rho=20$ mm, 30 mm and 40 mm. Although the power of our laser source did not represent any significant problem when used in phantoms, it may be harmful for in vivo applications; a discussion on this last point is given at the end of Section 4.2.2.

To retrieve the optical properties of the liquid layer from the three-layer experiment, a program written in Python containing the theory described in Section 2 was used, together with a fitting routine based on the Levenberg-Marquardt method [23]. The fitting procedure is explained in the scheme of Fig. 4; this fitting
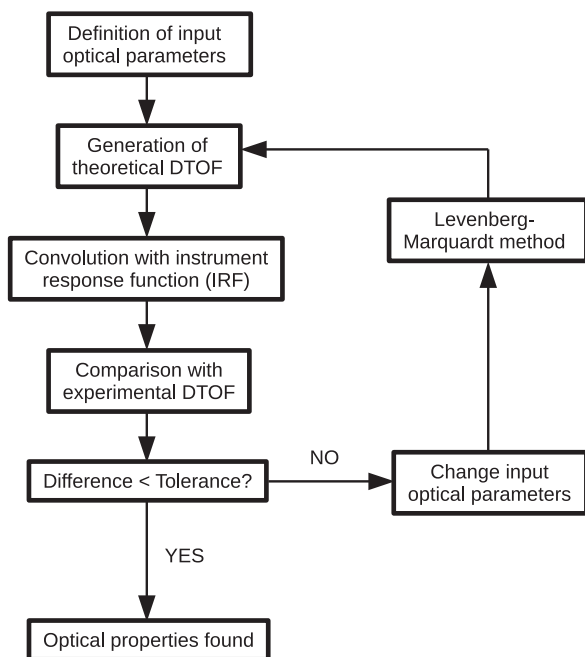
Fig. 4. Scheme for the fitting procedure used to retrieve the optical properties of the last layer in the three-layers experiment, as well as the optical properties of the first and second layers in the corresponding homogeneous experiments.

routine was also used to retrieve the optical properties of all the layers in corresponding homogeneous experiments, as stated in the preceding paragraph, but using the homogeneous model of Ref. [18] instead of ours. When solving the minimization problem, the optical properties $\left(\mu_{a,3}, \mu'_{s,3}\right)$ were limited to a range compatible with the optical properties of living tissue [24,25]. In detail, the absorption coefficient could take values in the range $0.002\ \text{mm}^{-1} < \mu_{a,3} < 0.03\ \text{mm}^{-1}$ and the reduced scattering coefficient could take values in the range $0.4\ \text{mm}^{-1} < \mu'_{s,3} < 2.0\ \text{mm}^{-1}$. It is also necessary to consider that in our experiment we used turbid parallelepipeds instead of cylinders, so in order to minimize numerical errors due to the different geometries, the radius of the cylinders used in the model was set to a value large enough to consider the medium as infinitely extended in the $x - y$ plane.

Due to the wide range of values associated with each optical parameter, as well as the high value of the cylinder radius and the source-detector distance, it was necessary to take a large number of frequencies (1024) and Bessel zeros (600) in order to build a sufficiently robust DTOF from the theoretical model. The resulting temporal range consisted of 1024 channels with a temporal step size of 16.29 ps.

3.2. Monte carlo simulations

Numerical Monte Carlo (MC) simulations were carried out for every combination of source-detector distance and ink concentration used in the measurements on phantoms, in order to validate our model independently from the experiments. Besides, this permits setting exact values for the optical properties of each layer without the typical uncertainties introduced by the measuring process.

The corresponding numerical DTOFs were obtained using a code taken from Ref. [26] and adapted to the specific necessities of this work. The code, which is implemented in the CUDA™ architecture, run on a NVIDIA® GTX480 graphics card. In each simulation, 2×10^{10} photons were launched, with a runtime between four and five hours. We payed special attention on reproducing the conditions of the previously described experiments: the simulated

medium was laterally large enough (compared with the used source-detector distances and its total thickness) to avoid influence of the boundaries, and all the layers had the same thicknesses as in the experiment (Table 1 in Section 4); the temporal range and the number of time channels were also reproduced here.

4. Results and discussion

4.1. Reference optical properties and thicknesses of each layer

Firstly, we analyzed separate measurements on the agarose blocks and on the milk solutions to obtain the reference optical properties of the three layers individually. The resulting absorption and reduced scattering coefficients of the solid layers, as well as their thicknesses, are listed in Table 1. The goal was to reproduce the typical values found in the upper layers of brain tissue ([24,25]). Note that, although both solid layers were prepared with the same mixture of milk and water, with the purpose of keeping μ'_s constant, we found in fact that $\mu'_{s,1} \neq \mu'_{s,2}$. This small discrepancy of less than 10%, is most probably due to the different ink concentrations used in each layer. Regarding the thicknesses, we aimed to achieve values of $d_1 = 7\ \text{mm}$ for the first layer and $d_2 = 5\ \text{mm}$ for the second layer, to fulfill a total thickness of $d = d_1 + d_2 = 12\ \text{mm}$, which lies in the range of values commonly found in literature ([27–29]). Nevertheless, the resulting thicknesses were of $d_1 = 5\ \text{mm}$ and $d_2 = 3\ \text{mm}$, making $d = 8\ \text{mm}$. This difference with respect to the aimed values is probably related to the solidification process of agarose, which involves heating the mixture almost to the boiling point of water, with the corresponding loss of some liquid volume due to evaporation. Although these quantities were lower than expected, we considered they were still adequate values for our experiments.

In Table 2 we show the optical properties of the liquid layer for each ink concentration. As stated above, we used the reflectance theory of Ref. [18] to fit the DTOFs measured in the semiinfinite homogeneous medium. The first three ink concentration steps were 0.8 ml/l, which led to a step in $\mu_{a,3}$ of $5 \times 10^{-4}\ \text{mm}^{-1}$. The last three ink concentration steps were 3.2 ml/l, corresponding to a step in $\mu_{a,3}$ of $\sim 2 \times 10^{-3}\ \text{mm}^{-1}$. The variation in $\mu'_{s,3}$ for the different ink concentrations led to a relative difference of $\sim 4\%$ between the first and the last value. Hence, we can say it remained almost constant.

Table 1
Thicknesses and optical properties of the solid layers.

	d (mm)	μ_a (mm^{-1})	μ'_s (mm^{-1})
1st layer	5 ± 0.1	$0.00311 \pm 2 \times 10^{-5}$	$0.789 \pm 5 \times 10^{-3}$
2nd layer	3 ± 0.1	$0.00447 \pm 4 \times 10^{-5}$	$0.719 \pm 7 \times 10^{-3}$

Table 2
Optical properties of the third layer for each ink concentration.

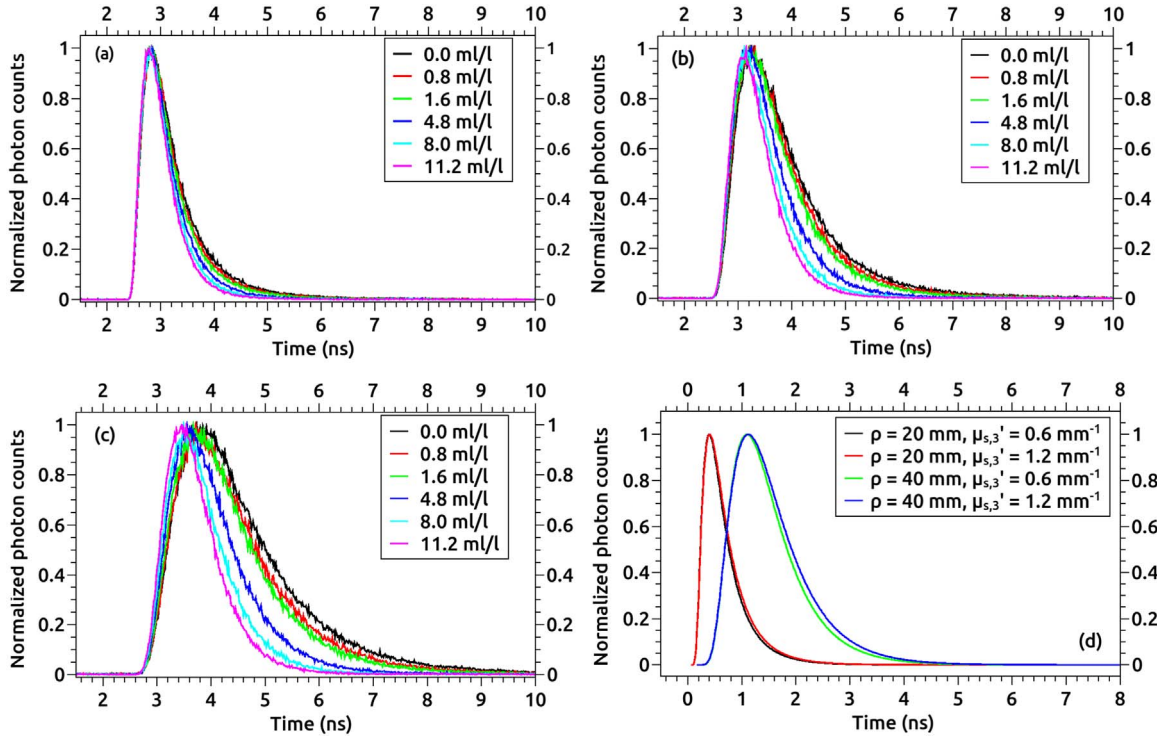| Ink concentration (ml/l)	$\mu_{a,3}$ (mm^{-1})	$\mu'_{s,3}$ (mm^{-1})
0.0 (no ink)	$0.00252 \pm 1 \times 10^{-5}$	$0.904 \pm 4 \times 10^{-3}$
0.8 ± 0.1	$0.00299 \pm 1 \times 10^{-5}$	$0.918 \pm 5 \times 10^{-3}$
1.6 ± 0.1	$0.00347 \pm 1 \times 10^{-5}$	$0.904 \pm 5 \times 10^{-3}$
4.8 ± 0.1	$0.00535 \pm 3 \times 10^{-5}$	$0.874 \pm 8 \times 10^{-3}$
8.0 ± 0.1	$0.00736 \pm 4 \times 10^{-5}$	$0.886 \pm 6 \times 10^{-3}$
11.2 ± 0.1	$0.00919 \pm 5 \times 10^{-5}$	$0.861 \pm 6 \times 10^{-3}$

Fig. 5. Comparison of the measured, normalized DTOFs for all six ink concentrations. a) ρ = 20 mm; b) ρ = 30 mm; c) ρ = 40 mm; d) simulated DTOFs for selected reduced scattering coefficients $\mu'_{s,3}$ (absorption fixed to $\mu_{a,3}$ = 0.0054 mm^{-1}, corresponding to ink concentration 4.8 ml/l).

4.2. Validation of the model and the fitting algorithm

4.2.1. Experiments on phantoms

Figs. 5a to 5c show the DTOFs measured in the three layer configuration for the various ink concentrations splitted by the three source-detector separations. We can see that the absorption of the third layer mainly affects the tail of the DTOF rather than the leading edge. It can be observed that the strongest changes are visible for the 40 mm source-detector separation. We did not vary the reduced scattering coefficient of the third layer in our experiments. Instead of that, Fig. 5d shows normalized theoretical DTOFs (obtained from Eq. (11)) for selected scattering properties of the third layer. Although it is a well known fact that, for homogeneous media, the variation in the reduced scattering coefficient principally affects the leading edge and the position of the maximum of the DTOFs [17], in the case of our layered model we observe changes in the tail of the pulses. However, this has only a small effect compared to absorption; i.e., relative changes in $\mu'_{s,3}$ have much less effects that relative changes of the same order in $\mu_{a,3}$. This result demonstrates that retrieval of $\mu'_{s,3}$ represents a much more difficult task than retrieval of $\mu_{a,3}$.

In order to derive the optical properties of the third layer from the measured DTOFs we started routinely with fitting of $\mu'_{s,3}$ and $\mu_{a,3}$ using arbitrarily chosen initial parameters. By means of this strategy we observed that the fitting routine did not find the true minimum of the χ^2 objective function in a large number of cases. Therefore, we systematically sampled the parameter space $\left(\mu_{a,3}, \mu'_{s,3}\right)$ in order to investigate whether the χ^2 objective function has a unique minimum.

In Fig. 6 we show three examples of calculated χ^2 plots, for every source-detector separation and for the third ink concentration in the liquid layer, as listed in Table 2. In each case, the green asterisk indicates the position of the minimum χ^2 value in the $\left(\mu_{a,3}, \mu'_{s,3}\right)$ space, while the red cross indicates the position of the true (reference) values according to the data shown in Table 2. The ideal situation would be that both marks overlap. Instead of that,

we see that the obtained $\mu_{a,3}$ is always underestimated, while the obtained $\mu'_{s,3}$ depends on the source-detector distance. For ρ = 40 mm it is properly obtained, while for ρ = 30 mm it is barely underestimated. In contrast, for ρ = 20 mm the objective function becomes smallest when $\mu'_{s,3}$ is at the high end of the considered parameter range. When we extend this range towards larger values, the retrieved $\mu'_{s,3}$ increases further. This behavior was observed for all investigated ink concentrations. This means that no reliable estimation of the reduced scattering coefficient can be obtained from the smallest source-detector separation.

Besides, in each plot we notice the presence of an extended blue region of low χ^2 values along the $\mu'_{s,3}$ axis, meaning that several reduced scattering coefficients may correctly represent the experimental data, although there is one unique minimum value. This result confirms the difficulties to accurately determine the reduced scattering coefficient of the third layer, as expected from the interpretation given above for Fig. 5.

To derive the final estimates of the third layer optical properties we used the pair $\left(\mu_{a,3}, \mu'_{s,3}\right)$ representing the minimum χ^2 value found from the systematic data space sampling as initial parameters for the fitting routine. Fig. 7 shows the optical properties obtained in this way versus ink concentration. The true parameters are represented by the black line. The utilized input parameters, $\left(\mu_{a,3}^{(0)}, \mu'^{(0)}_{s,3}\right)$, obtained from the χ^2 plots for all cases, are listed in Table 3. In Fig. 7a we see that the absorption coefficient is barely underestimated for all ink concentrations, except for the last one. In the case of $\mu'_{s,3}$ (Fig. 7b), the largest source-detector separation (ρ = 40 mm) yields the smallest deviation from the true values, in particular for the higher ink concentrations. For the smaller ink concentrations (1.6 ml/l and below) $\mu'_{s,3}$ is also well estimated for ρ = 30 mm. The mean partial pathlengths (MPPs) [6,8] of the travelling photons and, consequently, their average penetration depth, are reduced when absorption is increased. To compensate that, a larger interfiber distance is of advantage. This can be understood since for a given (limited) dynamic range of the DTOF that can be measured, the probability to detect photons with
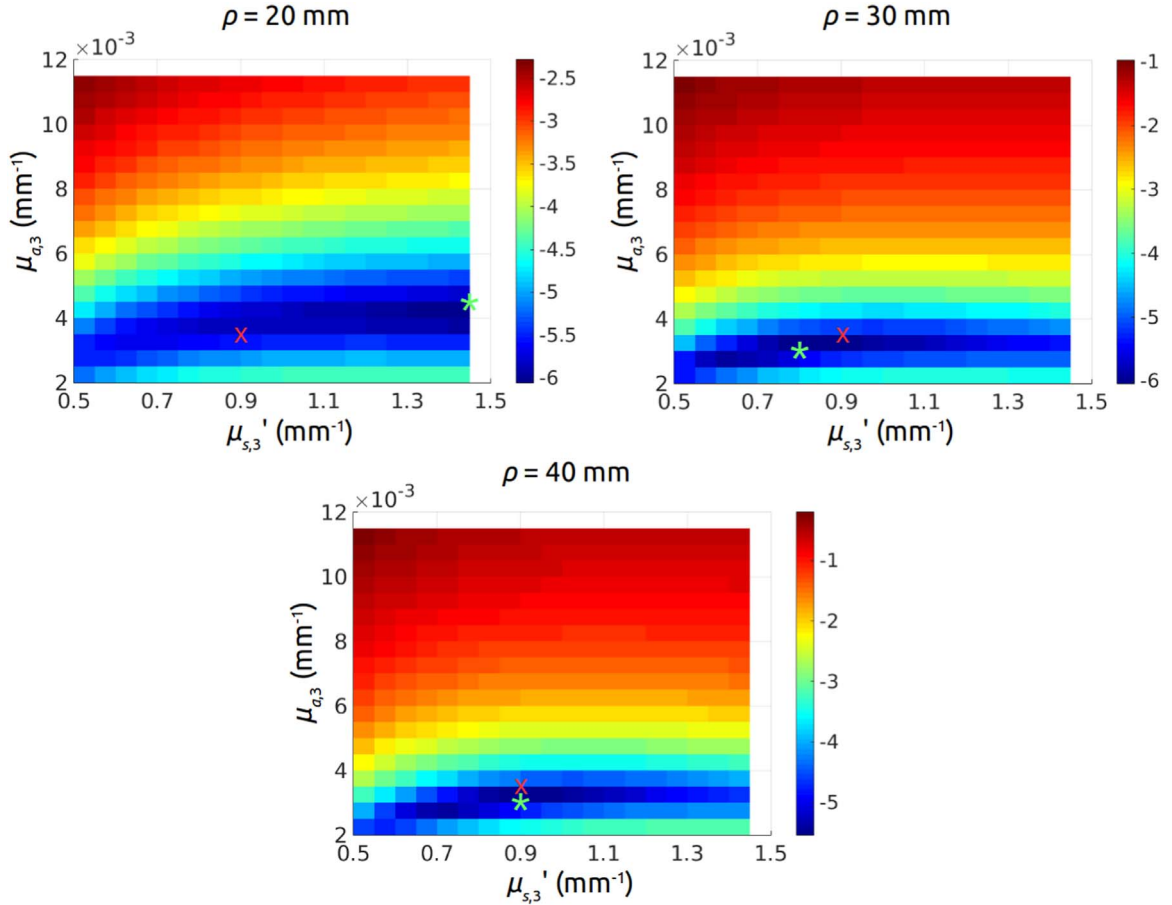
Fig. 6. Logarithmic χ^2 plots for $\rho = 20$ mm, 30 mm and 40 mm, and an ink concentration of 1.6 ml/l. The optical parameters were sampled as follows: initial $\mu_{a,3} = 0.002$ mm^{-1}, final $\mu_{a,3} = 0.012$ mm^{-1}, $\Delta\mu_{a,3} = 0.0005$ mm^{-1}; initial $\mu'_{s,3} = 0.5$ mm^{-1}, final $\mu'_{s,3} = 1.5$ mm^{-1}, $\Delta\mu'_{s,3} = 0.05$ mm^{-1}. The green asterisk indicates the position of the minimum χ^2 value, while the red cross indicates the position of the true (reference) optical parameters, according to the data shown in Table 2. (For interpretation of the references to color in this figure legend, the reader is referred to the web version of this article.)

longer mean pathlengths and hence with an increased penetration depth is higher for larger interoptode distances.

Finally, Fig. 8 shows the retrieved absorption coefficient of the third layer when $\mu'_{s,3}$ remains fixed at its real value, according to Table 2. We consider this an interesting situation since, in brain hemodynamics, absorption may suffer much higher changes than scattering, due to its dependence on chromophore concentrations [8,30]. The input value $\mu_{a,3}^{(0)}$ for each source-detector distance and for each ink concentration is listed in Table 3. For the lowest ink concentration in Fig. 8, the absorption coefficient is correctly retrieved for all the three source-detector distances, being $\rho = 20$ mm the one that gives the best result; for the second up to the fourth ink concentration, $\mu_{a,3}$ is better retrieved with $\rho = 30$ mm; and for the last two ink concentrations, $\rho = 40$ mm seems to work better than the other source-detector distances. When the ink concentration is increased, the well-known banana-shaped photon paths [31] tend to shorten and consequently information from the interior of the medium is no longer properly gathered. This is reflected in the quick breakdown of the accuracy with increasing ink concentration for $\rho = 20$ mm.

For $\rho = 30$ mm and $\rho = 40$ mm the penetration depth seems to be sufficient for all ink concentrations to characterize the third layer, and observed deviations from the true absorption coefficients arise mainly from experimental noise and probably from limitations of the model itself.

The results in Fig. 8 are based on the assumption that the reduced scattering coefficient of the third layer has been known. The χ^2 plots in Fig. 6 show that the resulting absorption coefficient will

essentially not change when a larger reduced scattering coefficient is applied, since the dark blue valley is almost horizontal in the right part of the Figures. This behavior is valid for the three smallest ink concentrations. Hence, a wrong assumption on the reduced scattering coefficient has almost no effect, provided that it has been chosen sufficiently large to fall in the horizontal part of the blue colored region in Fig. 6. In the case of the larger ink concentrations, the logarithmic χ^2 plots (not shown here) indicate that $\mu'_{s,3}$ and $\mu_{a,3}$ are more correlated in the range of the true values. This correlation becomes also visible when comparing Figs. 7 and 8. In Fig. 7b, several reduced scattering coefficients $\mu'_{s,3}$ are below the true values at the higher ink concentrations (see, e.g., green symbols in the right part of Figure 7b). To obtain the results in Fig. 8, these coefficients were substituted by the larger true values (black symbols in Fig. 7b). The corresponding absorption coefficients in Fig. 8 are larger than the original values in Fig. 7a. Hence, at higher ink concentrations it is of more importance to know the reduced scattering coefficient from the DTOFs, preferably retrieved at $\rho = 40$ mm.

4.2.2. Monte Carlo simulations

Fig. 9 shows MC DTOFs fitted with the algorithm described in Section 3, for $\rho = 30$ mm (Fig. 9a) and $\rho = 40$ mm (Fig. 9b), and for optical properties corresponding to the lowest (red) and highest (blue) ink concentrations listed in Table 2. The input optical parameters for this case were $\left(\mu_{a,3}^{(0)}, \mu'^{(0)}_{s,3} \right) = (0.009, 0.7)$ (mm^{-1}). In this analysis a delta pulse instrument response function was assumed. As can be seen from the legends in Fig. 9, in the worst
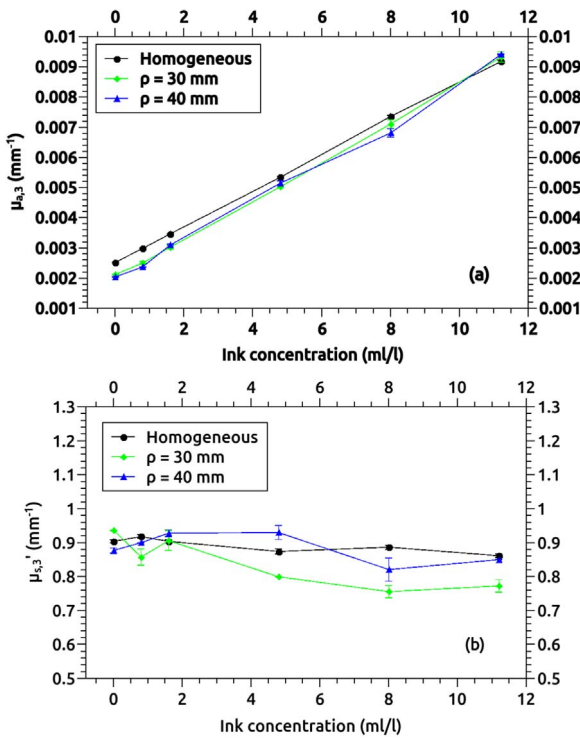
Fig. 7. Retrieved (a) absorption coefficient and (b) reduced scattering coefficient, of the third layer for all six ink concentrations and estimated from $\rho = 30$ mm and $\rho = 40$ mm. The black line represents the real values. Initial parameters for each case are listed in Table 3.

Table 3

Initial parameters, $\left(\mu_{a,3}^{(0)}, \mu_{s,3}^{\prime(0)}\right)$ (mm^{-1}), for the fitting routine, obtained from the χ^2 plots for all the three source-detector distances and six ink concentrations.

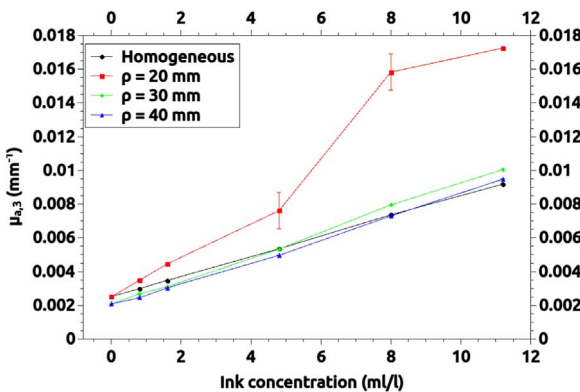| Ink concentration (ml/l)	$\rho = 20$ mm	$\rho = 30$ mm	$\rho = 40$ mm
0.0	(0.0020,1.45)	(0.0020,0.80)	(0.0020,0.85)
0.8	(0.0030,1.45)	(0.0025,0.80)	(0.0025,0.85)
1.6	(0.0040,1.45)	(0.0030,0.80)	(0.0030,0.9)
4.8	(0.0060,1.45)	(0.0050,0.80)	(0.0045,0.75)
8.0	(0.0085,1.45)	(0.0070,0.80)	(0.0065,0.75)
11.2	(0.0110,1.45)	(0.0090,0.80)	(0.0085,0.75)

Fig. 8. Retrieved absorption coefficient $\mu_{a,3}$ of the third layer for all six ink concentrations and three source-detector distances, with fixed $\mu'_{s,3}$. The black line represents the real values. The initial absorption coefficient for each fit is listed in Table 3.

situation ($\rho = 30$ mm and highest ink concentration) the retrieved optical parameters are well estimated, within 10% error. This difference can be appreciated in the plots as a deviation between the
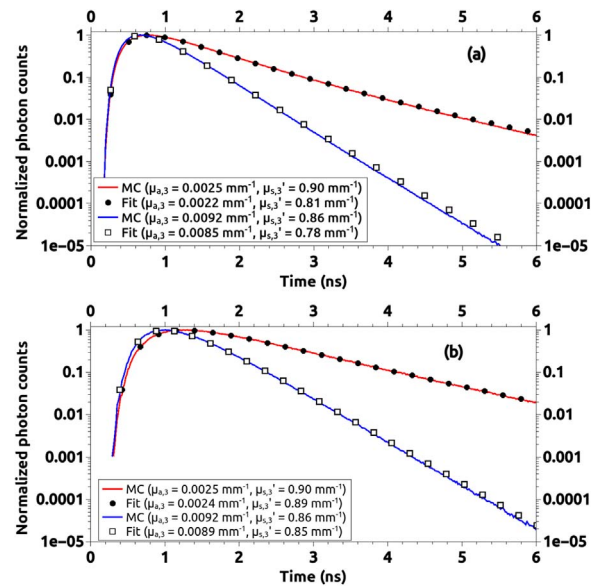

Fig. 9. Fit of DTOFs obtained by Monte Carlo simulations with the three-layer diffusion model, for (a) $\rho = 30$ mm and (b) $\rho = 40$ mm, and optical properties corresponding to the lowest (red) and highest (blue) ink concentrations listed in Table 2. The input parameters were $\left(\mu_{a,3}^{(0)}, \mu_{s,3}^{\prime(0)}\right) = (0.009, 0.7)$ (mm^{-1}). The true (MC) and the retrieved (Fit) optical parameters can be seen in the corresponding legends. (For interpretation of the references to color in this figure legend, the reader is referred to the web version of this article.)

simulated and the fitted DTOF, in the region of late detected photons (large time channels), and starts being noticeable just five orders of magnitude below the maximum of the DTOF, which is something that can hardly be achieved in real experiments. Better results were obtained for intermediate ink concentrations (which are not presented here for the sake of clarity).

As stated before, experiments on phantoms were performed using high fluences on the phantom surface, thus allowing short acquisition times. However, actual experiments in the clinic require much lower fluences at the skin to ensure that safety limits are not exceeded. Because of this, as an additional validation of our algorithm, we simulated MC pulses of very low total counts ($\sim 2.5 \times 10^5$ detected photons, in contrast with the previous simulations, for which the total counts were between 10^6 and 10^7), which are comparable or even below typical count values for *in vivo* applications [29]. Fig. 10 presents an example of a fitted DTOF, for $\rho = 40$ mm, $\mu_{a,3} = 0.003$ mm^{-1} and $\mu'_{s,3} = 1$ mm^{-1}. The input parameters were again $\left(\mu_{a,3}^{(0)}, \mu_{s,3}^{\prime(0)}\right) = (0.009, 0.7)$ (mm^{-1}). As it can be seen, the results of the fit demonstrate that even under this
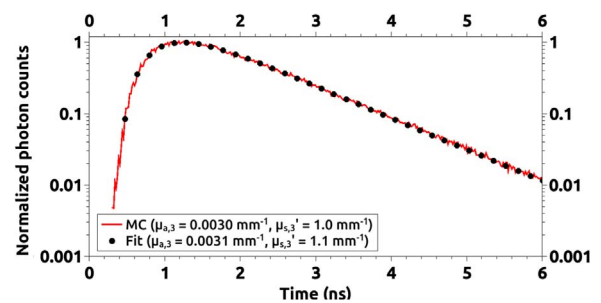

Fig. 10. Monte Carlo DTOF of low (2×10^5) photon counts fitted with the algorithm presented in Section 3, for $\rho = 40$ mm, with optical properties of the third layer $\left(\mu_{a,3}, \mu'_{s,3}\right) = (0.003, 1.0)$ (mm^{-1}). The input parameters were $\left(\mu_{a,3}^{(0)}, \mu_{s,3}^{\prime(0)}\right) = (0.009, 0.7)$ (mm^{-1}). The retrieved optical properties are given in the legend.

challenging experimental condition the algorithm is still robust and capable of retrieving the optical properties of the deepest layer, with an error of the same order than for DTOFs with much higher counts.

5. Conclusions

We developed an improved theoretical model for NIR light propagation in layered, turbid cylinders with an infinitely thick last layer, which leads to time domain expressions for the fluence $\phi(r, t)$ and the reflectance $R(\rho, t)$ at the top surface easier to calculate, and consequently computation times are reduced. Time-domain reflectance curves were obtained in typically less than 500 ms which is twice faster than the calculation times reported in the multilayer model of Ref. [11].

Our model was also implemented in a fitting algorithm, written in Python, in order to retrieve the optical parameters of the deepest layer from single distance, time-resolved diffuse reflectance measurements, leading to easier data analysis and processing than multi-distance measurements. Using a three layers phantom containing two solid, shallow layers and a third, liquid one, of variable absorption coefficient, DTOFs were acquired at source-detector distances of $\rho = 20$ mm, 30 mm and 40 mm. The DTOFs were fitted with both the absorption and the reduced scattering coefficients of the third layer as free parameters.

When using the data measured at $\rho = 30$ mm or $\rho = 40$ mm, we retrieved values for both coefficients with an error below 10% which, for this kind of experiments, is an acceptable value when compared with the results reported by other authors [7,12,14]. Systematic differences for both source-detector distances were obvious at higher absorption coefficients of the third layer. Here, its reduced scattering coefficient was best reproduced from $\rho = 40$ mm, whereas the smaller average penetration depth of the detected photons at $\rho = 30$ mm resulted in a moderate under-estimation of $\mu'_{s,3}$. The absorption coefficients from both distances were comparable.

Using systematic sampling of the χ^2 objective function for a reasonable range of optical properties, we observed that χ^2 becomes small for a large range of reduced scattering coefficients. As a consequence, when starting the fit with arbitrarily chosen initial parameters, the true minimum was often not found. Stable convergence to the minimum was obtained by taking the rough minimum position from the sampling grid as initial values $\left(\mu_{a,3}, \mu'_{s,3}\right)$ for the fit. For $\rho = 20$ mm the systematic sampling showed that this short distance does not yield sufficient information to reliably retrieve the optical properties of the third layer. This result was also confirmed when assuming the reduced scattering coefficient to be known and fitting only the absorption coefficient of the third layer. In this case, only the lowest absorption coefficient could be properly retrieved.

Finally, we carried out Monte Carlo simulations in order to test the model and the fitting algorithm independently from the experiments on phantoms. This was also helpful for choosing the optical and geometrical parameters without the typical erros introduced by the measurement processes. For both $\rho = 30$ mm and $\rho = 40$ mm, the absorption and the reduced scattering coefficient could be well retrieved, even for the proposed optical properties corresponding to the last ink concentration (with a maximum deviation of 10%). Since the number of counts of the respective pulses were rather high (between 10^6 and 10^7 detected photons), we also simulated a more realistic (and consequently challenging) situation, with only 10^5 detected photons, which is a more appropriate value for *in vivo* investigations. The fitting algorithm still correctly retrieved the optical properties of the third layer,

demonstrating that under such conditions it remains sufficiently robust.

Generally speaking, the weak dependence of χ^2 with the reduced scattering coefficient hampered its estimation with high accuracy, whereas the absorption coefficient could be more reliably estimated. A possible way to improve the results for the reduced scattering coefficient could comprise simultaneous exploitation of several source-detector distances. In this way, also changes in the amplitude of the DTOFs could be taken into account as additional information. Furthermore, measurements at even shorter distances could offer access to independently determine the optical properties of the upper layers, which were assumed to be known in our present analysis. From the experimental point of view, our next goal is to study a three-layered system with the second layer simulating the cerebrospinal fluid of the brain, i.e., to prepare this layer with small or zero scattering. Moreover, the studies presented here are restricted to only one wavelength, since absorption and scattering characteristics in phantoms do not suffer high variations in the NIR range; however, strong absorption dependence with λ in *in vivo* systems could permit the acquisition of additional information related to chromophore concentrations shuch as oxy- and deoxy-hemoglobin.

References

[1] Jöbsis F. Noninvasive, infrared monitoring of cerebral and myocardial oxygen sufficiency and circulatory parameters. Science 1977;198(4323):1264–1267. http://dx.doi.org/10.1126/science.929199.

[2] Strangman GE, Li Z, Zhang Q. Depth sensitivity and source-detector separations for near infrared spectroscopy based on the Colin27 Brain Template. PLoS ONE 2013;8(8):1–13. http://dx.doi.org/10.1371/journal.pone.0066319.

[3] Demel A, Feilke K, Wolf M, Poets CF, Franz AR. Correlation between skin, bone, and cerebrospinal fluid layer thickness and optical coefficients measured by multidistance frequency-domain near-infrared spectroscopy in term and pre-term infants. J Biomed Opt 2014;19(1):017004. http://dx.doi.org/10.1117/1.JBO.19.1.017004.

[4] Yoshitani K, Kawaguchi M, Miura N, Okuno T, Kanoda T, Onishi Y, et al. Effects of hemoglobin concentration, skull thickness, and the area of the cerebrospinal fluid layer on near-infrared spectroscopy measurements. Anesthesiology 2007;106(3):458–462. http://dx.doi.org/10.1097/00000542-200703000-00009.

[5] Dayan I, Havlin S, Weiss G. Photon migration in a two-layer turbid medium. A diffusion analysis. J Mod Opt 1992;39(7):1567–1582. http://dx.doi.org/10.1080/09500349214551581.

[6] Hiraoka M, Firbank M, Essenpreis M, Cope M, Arridge SR, van der Zee P, et al. A Monte Carlo investigation of optical pathlength in inhomogeneous tissue and its application to near-infrared spectroscopy. Phys Med Biol 1993;38:1859–1876.

[7] Kienle A, Patterson S, Dögnitz N, Bays R, Wagniéres G, van den Bergh H. Non-invasive determination of the optical properties of two-layered turbid media. Appl Opt 1998;37(4):779–791. http://dx.doi.org/10.1364/AO.37.000779.

[8] Steinbrink J, Wabnitz H, Obrig H, Villringer A, Rinneberg H. Determining changes in NIR absorption using a layered model of the human head. Phys Med Biol 2001;46:879–896. http://dx.doi.org/10.1088/0031-9155/46/3/320.

[9] Martelli F, Sassaroli A, Del Bianco S, Zaccanti G. Solution of the time-dependent diffusion equation for a three-layer medium: application to study photon migration through a simplified adult head model. Phys Med Biol 2007;52:2827–2843. http://dx.doi.org/10.1088/0031-9155/52/10/013.

[10] Liemert A, Kienle A. Light diffusion in N-layered turbid media: frequency and time domains. J Biomed Opt 2010;15(2):025002. http://dx.doi.org/10.1117/1.3368682.

[11] Liemert A, Kienle A. Light diffusion in a turbid cylinder. II. Layered case. Opt Express 2010;18(9):9266–9279. http://dx.doi.org/10.1364/OE.18.009266.

[12] Hallacoglu B, Sassaroli A, Fantini S. Optical characterization of two-layered turbid media for non-invasive, absolute oximetry in cerebral and extracerebral tissue. PLoS ONE 2013;8(5):1–15. http://dx.doi.org/10.1371/journal.pone.0064095.

[13] Martelli F, Del Bianco S, Spinelli L, Cavalieri S, Di Ninni P, Binzoni T, et al. Optimal estimation reconstruction of the optical properties of a two-layered tissue phantom from time-resolved single-distance measurements. J Biomed Opt 2015;20(11):115001. http://dx.doi.org/10.1117/1.JBO.20.11.115001.

[14] Martelli F, Del Bianco S, Zaccanti G. Procedure for retrieving the optical

properties of a two-layered medium from time-resolved reflectance mea-surements. Opt Lett 2003;28(14):1236–1238. http://dx.doi.org/10.1364/OL.28.001236.

[15] Jelzow A, Wabnitz H, Tachtsidis I, Kirilina E, Brühl R, Macdonald R. Separation of superficial and cerebral hemodynamics using single distance time-domain NIRS measurement. Biomed Opt Express 2014;5(5):1465–1482. http://dx.doi.org/10.1364/BOE.5.001465.

[16] Re R, Contini D, Zucchelli L, Torricelli A, Spinelli L. Effect of a thin superficial layer on the estimate of hemodynamic changes in a two-layer medium by time domain NIRS. Biomed Opt Express 2016;7(2):264–277. http://dx.doi.org/10.1364/BOE.7.000264.

[17] Patterson MS, Chance B, Wilson BC. Time resolved reflectance and transmit-tance for the non-invasive measurement of tissue optical properties. Appl Opt 1989;28(12):2331–2336. http://dx.doi.org/10.1364/AO.28.002331.

[18] Contini D, Martelli F, Zaccanti G. Photon migration through a turbid slab de-scribed by a model based on diffusion approximation. I. Theory. Appl Opt 1997;36(19):4587–4599. http://dx.doi.org/10.1364/AO.36.004587.

[19] Poularikas, AD. (editor), The transforms and applications handbook: Second edition, CRC Press, Boca Raton, 2000.

[20] Martelli F, Del Bianco S, Ismaelli A, Zaccanti G. Light propagation through biological tissue and other diffusive media. Theory, solutions, and software. Bellingham, Washington: SPIE Press; 2010.

[21] Haskell RC, Svaasand LO, Tsay TT, Feng TC, Mc Adams MS, Tromberg BJ. Boundary conditions for the diffusion equation in radiative transfer. J Opt Soc Am A 1994;10:2727–2741. http://dx.doi.org/10.1364/JOSAA.11.002727.

[22] Cubbedu R, Pifferi A, Taroni P, Torricelli A, Valentini G. A solid tissue phantom for photon migration studies. Phys Med Biol 1997;42(10):1971–1979. http://dx.doi.org/10.1088/0031-9155/42/10/011.

[23] Marquardt D. An Algorithm for Least-Squares Estimation of Nonlinear Parameters. J Soc Ind Appl Math 1963;11(2):431–441. http://dx.doi.org/10.1137/0111030.

[24] Vo-Dinh, T. (editor), Biomedical photonics handbook, CRC Press, Boca Raton, London, New York, Washington, (2003).

[25] Bevilacqua F, Piguet D, Marquet P, Gross J, Tromberg B, Depeursinge C. In vivo local determination of tissue optical properties: applications to human brain. Appl Opt 1999;38(22):4939–4950. http://dx.doi.org/10.1364/AO.38.004939.

[26] Alerstan E, Svensson T, Anderson-Engels S. Parallel computing with graphics processing units for high speed monte carlo simulation of photon migration. J Biomed Opt 2008;13(6):060504. http://dx.doi.org/10.1117/1.3041496.

[27] Okamoto M, Dan H, Sakamoto K, Takeo K, Shimizu K, Kohno S, et al. Three-dimensional probabilistic anatomical cranio-cerebral correlation via the inter-national 10-20 system oriented for transcranial functional brain mapping. Neu-roimage 2004;21(1):99–111. http://dx.doi.org/10.1016/j.neuroimage.2003.08.026.

[28] Okada E, Delpy DT. Near-infrared light propagation in an adult head model. II. Effect of superficial tissue thickness on the sensitivity of the near-infrared spectroscopy signal. Appl Opt 2003;42(16):2915–2922. http://dx.doi.org/10.1364/AO.42.002915.

[29] Zucchelli L, Contini D, Re R, Torricelli A, Spinelli L. Method for the dis-crimination of superficial and deep absorption variations by time domain fNIRS. Biomed Opt Express 2013;4(12):2893–2910. http://dx.doi.org/10.1364/BOE.4.002893.

[30] Leung TS, Tachttsidis I, Tisdall M, Smith M, Delpy DT, Elwell CE. Theoretical investigation of measuring cerebral blood flow in the adult human head using bolus Indocyanine Green injection and near-infrared spectroscopy. Appl Opt 2007;46(10):1604–1614. http://dx.doi.org/10.1364/AO.46.001604.

[31] Feng S, Zeng F, Chance B. Photon migration in the presence of a single defect: a perturbation analysis. Appl Opt 1995;34(19):3826–3837. http://dx.doi.org/10.1364/AO.34.003826.